Longitudinal phase space characterization of the blow-out regime of rf photoinjector operation

J. T. Moody, P. Musumeci,* M. S. Gutierrez, J. B. Rosenzweig, and C. M. Scoby

Department of Physics and Astronomy, University of California at Los Angeles, Los Angeles, California 90095, USA

(Received 27 April 2009; published 29 July 2009)

Using an experimental scheme based on a vertically deflecting rf deflector and a horizontally dispersing dipole, we characterize the longitudinal phase space of the beam in the blow-out regime at the UCLA Pegasus rf photoinjector. Because of the achievement of unprecedented resolution both in time (50 fs) and energy (1.0 keV), we are able to demonstrate some important properties of the beams created in this regime such as extremely low longitudinal emittance, large temporal energy chirp, and the degrading effects of the cathode image charge in the longitudinal phase space which eventually leads to poorer beam quality. All of these results have been found in good agreement with simulations.

DOI: 10.1103/PhysRevSTAB.12.070704 PACS numbers: 29.25.Bx, 29.27.Bd, 41.75.Ht, 41.85.Ct

I. INTRODUCTION

The generation of high brightness beams by rf photoinjectors has been a fundamental advance in electron beam sources, having enabled many novel electron beam applications such as self-amplified spontaneous emission free-electron lasers (FELs) [1,2], inverse Compton scattering sources [3], and ultrafast relativistic electron diffraction [4,5]. The optimization for higher beam brightness typically involves proper shaping of the laser pulses at the photocathode [6,7]. Recently at the UCLA Pegasus photoinjector laboratory, we have experimentally demonstrated the blow-out regime of rf photoinjector operation. In this scheme, proposed a few years ago [8,9], a very short (< 100 fs) laser pulse illuminates the cathode and the beam expands under its own self-forces from its initial pancake-like shape to create a nearly ideal uniformly filled ellipsoidal distribution [10]. The main advantage of such a final state is that the beam self-fields are approximately linear in each of the coordinate offsets, resulting in extremely linear beam dynamics and phase spaces [11].

In general, while the physics of high brightness beam sources has been investigated in detail [12–14] it is noticeable that much of the theoretical and experimental attention has been given to the evolution of the transverse beam parameters, in particular beam sizes and normalized emittances, in the initial space charge dominated regime. The beam longitudinal phase space (LPS), which for some applications (for example, the free-electron laser) may be as important as the transverse phase space, has often been neglected. For example, only an upper limit has been established for the uncorrelated energy spread (or slice energy spread) of a beam directly after emission and acceleration by an rf photoinjector [15,16].

This inattention to longitudinal dynamics has been mostly due to the lack of adequate experimental techniques that simultaneously quantify the longitudinal momentum and temporal distributions of the bunch with sufficient resolution. Recently it has been recognized that by using a dispersing dipole in conjunction with a orthogonally deflecting rf cavity one could get a detailed picture of the beam longitudinal phase space [17,18]. A number of experimental groups have produced interesting results with this setup [19]. A growing number of high brightness beam facilities foresee the installation of a deflecting cavity to perform this measurement [20,21].

Being able to quantify the LPS is particularly important in the case of the blow-out regime, as one of the attractive characteristics of this scheme is that the linearity of the forces determining the beam evolution yields very linear phase space distributions, offering the possibility for strong compression factors. In this regard, we observe the advantages of the blow-out regime over the other proposed operating points of the rf photoinjector. Although the longitudinal space charge expansion during beam propagation increases the longitudinal emittance from the thermal level, the beam quality degradation is mitigated by the linearity of the dynamics. The final beam distribution is characterized by a significantly lower longitudinal emittance than other regimes of rf photoinjector operation. These considerations make the blow-out regime a very attractive option when considering recently proposed methods for emittance exchange between transverse and longitudinal phase spaces [22].

In this paper we report on the characterization of the blow-out regime of rf photoinjector operation by measurements of longitudinal phase space performed at the UCLA Pegasus laboratory. A significant experimental effort has been mounted to develop a diagnostic with enough resolution to measure both the small longitudinal emittance and the uncorrelated energy spread of the beam. The coupling between the transverse position and the beam energy introduced by the deflector, quantified by the Panofsky-Wenzel theorem, requires particular attention. The experimental solution that we have adopted is to use a horizontal slit to limit the vertical beam size in the deflector. Other

*musumeci@physics.ucla.edu

significant aspects of the results discussed here include verification that rf focusing in the gun has a limited effect when the initial laser pulse length is very short. A detailed study of the beam energy chirp in the final state reveals a relatively weak dependence on the beam charge, suggesting that a following magnetic compression stage (a negative R56 beam line) could recompress the beam with fixed magnet settings, not dependent on the shot-to-shot charge fluctuations. Finally, the longitudinal phase space presents very clear signs of distortion when the image charge field is large enough to break the symmetry of the space charge driven expansion.

Particle simulations performed by the general particle tracer (GPT) and measured results are both in reasonably good agreement with a simple analytical pancake model, confirming our understanding of the relatively simple beam dynamics in this regime.

In the next section we describe the experimental apparatus and the longitudinal phase space diagnostics employed. We then move on to discuss the systematic errors introduced in the measurement (in particular by the deflecting cavity). We are then able to show the results and the comparison with simulations.

II. EXPERIMENTAL SETUP

The beam line for the measurement of the longitudinal phase space is shown in Fig. 1. In order to generate a uniformly filled ellipsoidal distribution at the UCLA Pegasus laboratory we illuminate the cathode of a 1.6 cell SLAC/UCLA/BNL rf gun with a very short (< 50 fs rms) UV (266 nm) laser pulse. We refer to our previous publication on the blow-out regime operation of a photoinjector [10] for the details of the beam distribution characterization. The gun is operated for this measurement at a slightly lower accelerating gradient (75 MV/m) due to the lower rf power output from an aging klystron.

An X-band ($f = 9.599$ GHz) rf cavity with deflecting voltage V_0 up to 500 kV is used to establish a correlation between the beam time coordinate and the vertical plane

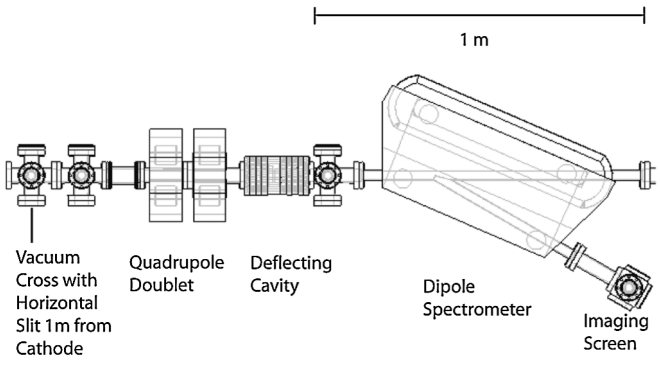

FIG. 1. Top down view of the Pegasus LPS measurement beam line section. The beam is sliced, focused, deflected, dispersed, and finally imaged.

[23]. The deflecting voltage streaks the beam, imbuing a transverse kick on each particle according to the phase it enters the cavity. By phasing the rf in the cavity so that the time centroid of the beam experiences no kick (zero phase), the longitudinal coordinate is thereby linearly mapped to the vertical transverse dimension on a fluorescent screen located downstream. In our previous paper [10], the deflector was used to retrieve the $t - x$ ellipsoidal beam distribution. Exploiting the two dimensional nature of the images obtained with the rf deflector, the horizontal coordinate can be used to encode any information whose variation along the bunch temporal coordinate is under study. Examples include the position and amplitude of a Bragg diffraction peak for ultrafast electron diffraction studies, or the beam size after a horizontally focusing quadrupole for slice emittance measurements [24]. Here we utilize the unstreaked dimension to display the momentum spectrum of the beam after it is dispersed by a magnetic dipole.

The dipole magnet employed has a design bend of 45 degrees and a radius of curvature of 0.67 m. After a distance $z = 29$ cm from the exit of the dipole, chosen in order to maximize the energy resolution and the screen energy acceptance, the transverse $x - y$ profile of the beam containing the mapped longitudinal phase space is imaged onto a $1''$ yttrium aluminum garnet (YAG) fluorescent screen from Radiabeam Technologies IBIS profile monitor.

For all measurements described in this paper, the emittance compensation solenoid is employed to guide the beam to a very gentle focus a few meters downstream of the cathode. Other important components of the measurement are shown in Fig. 1. A 100 μm wide horizontal aperture at a distance $z = 1$ m from the cathode is used to select a central slice of the beam to perform the measurement. The need for this experimental procedure arises from consideration of the effects of the deflecting electromagnetic field on the beam energy distribution and it is discussed in detail in the next section of this paper. The small aperture reduces the charge to $<5\%$ of its initial value, thus effectively stopping any further space charge driven dynamical evolution [25]. This is confirmed by GPT simulations. For photoinjector parameters typical of the measurements described in the paper, in the region after $z = 1$ m the energy spread would slightly (10%) increase. On the other hand, when the collimating slit aperture is inserted in the beampath, the simulated energy spread remains constant. This can be explained noting that even though the local charge density remains unmodified by the aperture, the beam aspect ratio and hence the magnitudes of the space charge forces in the transverse and longitudinal direction are strongly affected.

The only longitudinal phase space transformation that takes place after the slit is a drift propagation up to the deflecting cavity plane where the beam longitudinal profile gets imprinted by the transverse deflecting kick into the vertical plane.

Two quadrupole magnets of effective length $l_q = 10.4$ cm located, respectively, at $z = 1.54$ m and $z = 1.66$ m from the cathode are used to minimize the betatron beam sizes both in x and y at the measurement screen. The measured y-spot size on the YAG screen is <100 μm. Obtaining a well resolved LPS measurement requires that these beam sizes be small compared to the streaked and dispersed spot dimensions.

The temporal calibration at the measurement screen can be obtained using a deflector thin kick model. In this approximation, the proportionality factor between the vertical position of a particle in the beam at the imaging screen and its longitudinal position at the entrance of the rf cavity is given by

$$K = \frac{keV_0}{\gamma m_0 c^2 \beta} L, \tag{1}$$

where k is $\frac{2\pi f}{c}$, V_0 is the deflecting voltage, e and m_0 the electron charge and mass, γ and β the Lorentz factor and normalized velocity, respectively, and $L = 110$ cm is the drift distance from the center of the deflecting cavity to the imaging screen. As an example, for the LPS measurement vs charge discussed in the next section where the deflector was operated at $V_0 = 100$ kV, we obtained $K = 6.3$. Taking into account a camera calibration of 31 μm/pixel gives a calibration value of 16 fs/pixel.

This value is cross-checked with a direct measurement of the calibration factor obtained by lowering the deflecting voltage to a level in which a full phase sweep of the rf field can be observed on the measurement screen. The vertical centroid of the beam is then measured as a function of the phase of the deflecting cavity. The slope of the resulting sinusoidal variation at the zero crossing yields the pixel to phase calibration. The slope is then scaled by the ratio of the operating voltage and the phase sweep voltage as measured with an independent power meter and finally divided by kc to obtain the time calibration for a single pixel on the CCD. For the LPS vs charge measurement case, this method yielded a (15 ± 1) fs/pixel calibration in close agreement with the value predicted using Eq. (1).

The screen momentum calibration can be estimated using linear matrix transport analysis. The horizontal deviation from the design trajectory due to dispersive terms is

$$x = [\rho(1 - \cos\theta_b) + L_d \sin\theta_b]\frac{\delta\gamma}{\gamma}, \tag{2}$$

where ρ is the bending radius, θ_b the bending angle, and $L_d = 29$ cm is the drift distance from the exit of the dipole to the imaging screen. Again, taking into account the camera magnification, this gives a 270 eV/pixel calibration.

In order to verify this experimentally we measured the shift in the horizontal centroid of the beam when varying the magnetic field in the dipole magnet by a small amount, noting that a small variation $\delta B/B$ is equivalent to $-\delta p/p$. A linear fit gives (0.0073 ± 0.0003)%/pixel calibration factor. For a central beam energy of 3.55 ± 0.05 MeV this corresponds to (260 ± 10) eV/pixel in close agreement with our estimate.

A. Analysis of LPS images

Applying the calibrations discussed above to the raw image data from the digital camera, a direct measurement of the longitudinal phase space beam distribution is obtained. In order to simplify the description of the physics of the blow-out regime, we break down the characterization of the LPS to a few essential physically relevant parameters. These are the energy chirp that describes the correlated energy spread of the beam denoted by C, the rms energy spread (σ_{dE}), the rms bunch length (σ_t), the slice or uncorrelated or slice energy spread (σ_{dE_s}), and lastly the longitudinal phase space area or longitudinal emittance ($\epsilon_{z,n}$). Depending on the application each one of these parameters may be more important than the others. Ultimately, only the complete phase space distribution fully describes the beam, but these parameters can give insight into important physical processes inherent to the photoinjector blow-out regime.

The image analysis is performed by a National Instruments LABVIEW + MATLAB based routine and starts by filtering the raw image data. As in transverse phase space reconstruction measurements, filtering the noise is a critical issue in determining the phase space area [26,27]. The only difference in this case is that the raw image (with proper calibration applied) directly carries the longitudinal beam distribution information. As this method involves no numerical reconstruction in the data except rescaling the axes from $x - y$ to $p - z$, the filtering problem is simplified.

The filtering method proceeds as follows. An upper limit threshold is first applied to eliminate any saturated pixels that have resulted from x rays hitting the imaging camera CCD. After selecting a region of interest, an iterative rms cut is applied line by line until the computed beam rms values converge within a threshold of 0.1%. Finally, the filtered image is integrated in the two transverse dimensions over the region of interest. A lower bound threshold is applied until the total integrated intensity is decreased to 90% of its initial value to eliminate the noise contribution at the tails of the beam profile.

The beam chirp (C) is determined by slicing the beam in 50 fs slices for one rms bunch length around the beam centroid. The centroid of each slice is then computed and slope is determined by a linear least squares regression. The thickness of the distribution in each slice gives a local measure of the uncorrelated energy spread. The rms bunch length and energy spread are calculated by projecting the full image intensity distribution on the two correspondent axes. Finally, the normalized longitudinal emittance, which quantifies the area occupied by the beam in the longitudi-

nal phase space [28], can be computed by

$$\epsilon_{z,n} = \frac{\sqrt{\langle \delta z^2 \rangle \langle \delta p^2 \rangle - \langle \delta z \delta p \rangle^2}}{m_0 c}, \tag{3}$$

where δz and δp are the deviations of the particle longitudinal position and momentum from the respective mean values. It is of interest to comment about the choice of the units for the longitudinal emittance. While other appropriate unit choices exist, we have decided to normalize the phase space area to the electron mass and express the longitudinal emittance in terms of mm mrad. This has the immediate advantage of allowing direct comparison with the transverse emittance.

III. EXPERIMENTAL VERIFICATION OF THE PANOFSKY-WENZEL THEOREM IN THE DEFLECTING CAVITY

The most substantial source of systematic error in our measurement setup is the deflecting cavity. Use of a deflecting cavity to measure the longitudinal profile of an electron beam imposes an additional energy spread for off-axis particles. This additional energy spread is well described by the Panofsky-Wenzel theorem [29] which in its differential form can be written as [28]

$$\nabla_\perp (\Delta p_z) = \frac{\partial (\Delta \vec{p}_\perp)}{\partial z}. \tag{4}$$

Equation (4) indicates a relationship between the transverse momentum imparted to particles that are longitudinally off the center of phase of the beam, and the longitudinal momentum imparted to particles that are transversely off center of the axis of symmetry. When applied to a deflecting cavity the Panofsky-Wenzel theorem implies that the same factor that causes the deflection of the beam induces an increase in energy spread which depends on the transverse beam width inside the deflecting cavity.

By using a thin kick approximation, the energy change of an off-axis particle due to the rf fields of the deflector can be written, following Eq. (4), as

$$\frac{d\gamma}{\gamma} = \frac{keV_0}{\gamma m_0 c^2 \beta} y, \tag{5}$$

where y is the vertical particle position. The rest of the parameters are the same as those of Eq. (1). When applied to the second moment of the beam distribution, Eq. (5) describes the expected increase in energy spread in terms of the rms vertical beam size at the deflecting cavity.

An experimental study of the effect of energy spread imposed upon the electron beam by the deflecting cavity is shown in Fig. 2. A measurement of the increase in energy spread as a function of vertical spot size was performed by using the solenoid as a lens to change the transverse profile of the electron beam as it traveled through the deflecting cavity. The energy spreads for each spot size in Fig. 2 were normalized by the energy spread measured without any deflecting voltage, as changing the beam focusing has also an effect on the beam energy spread. The data is compared with the normalized quadrature sum of the measure initial energy spread and the induced contribution calculated using Eq. (5). The data is in good agreement with the kick model for the deflecting cavity, demonstrating the effect predicted by the Panofsky-Wenzel theorem on the beam energy spread.

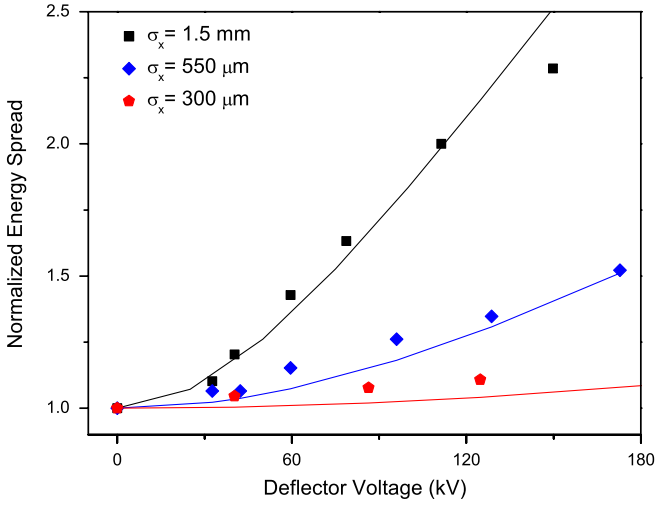

FIG. 2. (Color) A study of the Panofsky-Wenzel theorem in the deflecting cavity. The normalized energy spread is plotted versus the deflecting voltages for a given transverse spot size in the cavity shown as points are compared to the analytical result of a deflecting kick shown by lines.

This study motivated the use of an aperture in order to minimize the beam transverse dimensions in the deflecting cavity. Because of the deflecting mode field profile [23], the field gradient is maximum in the vertical axis and minimal along the horizontal axis. Hence, a horizontal aperture is used to minimize the induced additional energy spread. When the 100 μm wide slit is inserted, the energy spread of the beam on the spectrometer screen increases by approximately 600 eV with the deflector turned on at 100 kV with respect to the unstreaked beam. Although this value may be negligible when considering the total energy spread of the beam, the contribution from the deflecting cavity constitutes an additional uncorrelated energy spread, which limits the resolution of the measurement of this parameter at about 1 keV.

Given the low charge, the beam distortions that could arise from wakefields produced by the interaction between the beam and the slit are negligible.

IV. RESULTS AND COMPARISON WITH SIMULATION

A direct measurement of the LPS of a typical beam generated by the Pegasus photoinjector operated in the

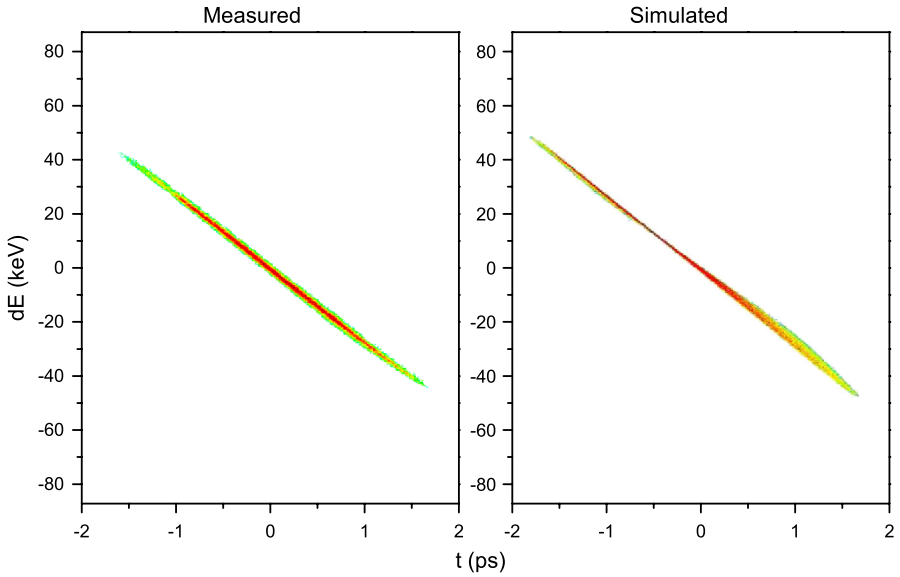

FIG. 3. (Color) Single shot LPS measurement compared with simulation. The filtered image data (shown on the left) has time on the vertical axis and the energy on the horizontal axis. The right figure shows the simulated results of the LPS by general particle tracer.

"blow-out" mode is shown in Fig. 3. For this measurement the laser spot on the cathode σ_l was 500 μm rms, the launch phase 22 degrees, and the charge $Q = 20$ pC. The measured LPS is quite linear and has a very low longitudinal emittance. These results are expected for the uniformly filled ellipsoidal beam distribution, which is characterized by space charge forces being linear as a function of all three coordinates measured from the bunch center. For photoinjector operating modes which involve the use of longer laser pulses on the cathode (> 3 ps), the LPS beam distribution would be characterized by a significant second order component due to the rf curvature. In the blow-out case, due to the linearity of the dynamics, it is the thickness of the energy distribution at a constant time relative from the bunch center, or uncorrelated energy spread, which determines the final longitudinal emittance. For this reason, the resolution of the LPS, which sets a limit on the minimum recordable linewidth is crucial in this measurement. The measured longitudinal emittance for the case shown in Fig. 3 is 0.5 ± 0.1 mm mrad. We observe, as suggested in [30], that the high beam quality of the phase space implies the feasibility of very large compression ratios.

In order to benchmark our understanding of the beam evolution, we compared the measurement with particle tracking simulations from GPT. The simulations start from the cathode and use a 2.5D field map for the rf gun and the on-axis magnetic measurement map for the emittance compensation solenoid. The beam dynamics is followed by GPT up to the slit plane. At this point a linear drift propagation matrix transformation up to the rf deflector plane is applied to the particle coordinates. Space-charge forces are not taken into account for this region of propagation as the slit has removed most of the beam charge.

We compare the resulting particle coordinates in the time-energy plane with the data. The simulation results obtained with GPT are also shown in Fig. 3 and are in remarkably good agreement with the data. There are essentially no free parameters in the simulation as the initial transverse and longitudinal spot size are taken from the laser measurements. A small degree of uncertainty is given by the nonuniform emission at the cathode which alters the beam spatial distribution and can thus affect the creation of the final state, causing some deviation from a uniformly filled ellipsoidal beam.

In Table I we summarize the longitudinal phase space parameters measured and compared with the simulation.

A significant characteristic of the measured longitudinal phase space is the strong correlation between energy and position along the bunch, i.e., energy chirp which is quantified with the chirp parameter $C = 90\ \frac{\mathrm{keV}/c}{\mathrm{mm}}$. This large correlation is due the final beam state being the result of a strong space charge driven expansion so that particles at the head of the beam have been pushed further and hence have higher energy. In order to obtain an analytical estimate, we observe that in the pancake approximation limit

TABLE I. LPS parameter comparison.

Parameter	Simulated	Measured	Unit
C	91	90 ± 1	keV/c mm
$\epsilon_{z,n}$	0.3	0.5 ± 0.1	mm mrad
σ_{dE}	22	21 ± 2	keV
σ_t	797	788 ± 8	fs

(beam in its own rest frame much smaller than its transverse width), the bunch length is given by $\tau = m_0 c\sigma/e\epsilon_0 E_0^2$, where $\sigma = Q/2\pi\sigma_l^2$ is the surface charge density at emission and E_0 the accelerating gradient [8]. The beam energy spread in the same approximation is given by $m_0c^2\Delta\gamma = e\sigma L_s/\epsilon_0$, where $L_s = 5$ cm is the length over which the space charge forces act. The distance $L_s = 5$ cm which gives a good estimate for the propagation region where the expansion takes place has been taken from the simulations as the point where the aspect ratio in the beam rest frame changes from an oblate to a prolate ellipsoid. A correct approach that takes into account the transition between the different regimes where the longitudinal and transverse space charge forces dominate the dynamics, respectively, at least in the nonrelativistic limit, is offered in Ref. [31]. Here we limit ourselves to a simple heuristic model. In the drift region following the gun, the energy spread stops increasing since the beam has become long in its rest frame and the residual elongation comes from the previously imprinted difference in beam velocities. The final bunch length is then $\tau_f = \tau + \Delta\gamma L_d/\gamma^3 c$, where L_d is the drift length to the deflecting cavity plane. The resulting final chirp is

$$C \cong m_0c^2 \frac{\Delta\gamma}{c\tau_f} \approx 85 \ \frac{\text{keV}}{\text{mm}} \tag{6}$$

in close agreement with the value found experimentally.

By calculating the rms energy spread on 50 fs temporal slices we obtain the result shown in Fig. 4 which displays the local slice or uncorrelated energy spread along the bunch. This quantity determines how cold the beam distribution is locally and is a critical beam parameter for many applications since it determines the growth rate of any beam instability, both desired like FEL amplification and harmful to the beam quality such as, for example, coherent synchrotron radiation instability. In current short-wavelength FEL injector designs, a laser heater is usually introduced in the beam line to be able to externally control the uncorrelated energy spread and damp the undesired instabilities [32].

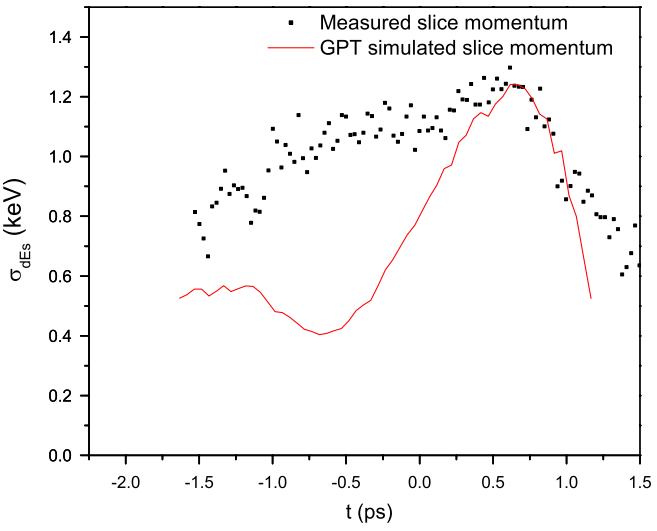

FIG. 4. (Color) The measured and simulated 50 fs slice energy spread along the bunch. The energy resolution of the measurement is limited to 1 keV.

Examining Fig. 4 we note that, although we cannot resolve the very small local slice energy spread of the central region of the beam, the measured slice energy spread follows the simulation for values larger than 1.0 keV. This is an indication of the resolution of the measurement. The 1.0 keV measured slice energy spread corresponds to a 0.027% relative energy spread and is, in absolute value, the lowest uncorrelated energy spread measured to date from an rf photoinjector beam.

We note that this is still much larger than the thermal spread of the particles coming out of the cathode. Consequently, the measured longitudinal emittance is at least 2 orders of magnitude larger than the thermal limit (in striking contrast with transverse emittances obtained from rf photoinjectors that are within a factor of 2 from the corresponding thermal limit).

The source of the uncorrelated or slice energy spread is primarily due to radial-energy correlations in the beam dynamics. The space charge field of a uniformly filled ellipsoidal charge distribution has ellipsoidal equipotential surfaces and hence a slice (a plane at constant z) contains particles at different energies. This accounts for most of the keV-level slice energy spread seen in the measurements and simulations.

Another effect which has to be taken into account is the radial dependence of the rf accelerating field. This is calculated from GPT simulations for the SLAC/UCLA/BNL 1.6 cell gun at 100 MV/m gradient to be 1 keV rms energy spread per 1 mm rms laser spot size on the cathode, in full agreement with the value reported in [33]. This quantity is proportional to the square of the rms laser spot size, so for a 400 μm rms spot size at the cathode (Pegasus nominal parameter) this contribution is <0.2 keV.

An estimate for the resolution can be obtained by measuring the vertical spot size before turning the rf deflector on for streaking. With the proper quadrupole settings, the spot size is found to be 87 μm rms or 2.8 pixel rms. Taking into account the large beam chirp of 90 $\frac{\text{keV}/c}{\text{mm}}$ or 30 keV/ps, this accounts for 1.1 keV energy uncertainty in agreement with the limit set by Fig. 4.

We have further characterized the behavior of the longitudinal phase space as a function of various photoinjector parameters. In Fig. 5 the variation of the main LPS parameters obtained by changing the injection phase is shown. Both the rms bunch length and the energy chirp show a very weak dependence on the rf phase. It has been pointed out [34] that by lowering the laser launch phase the gun acts as an rf compressor. This behavior is not observed

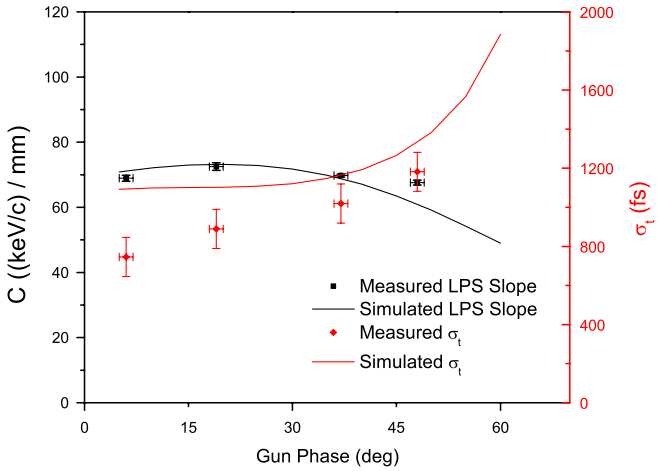

FIG. 5. (Color) A scan of the chirp (C) (left axis, black) and σ_t (right axis, red) versus rf gun phase. The measured values (points) are compared to simulations performed with general particle tracer. The scan was performed with a 20 pC electron beam with an initial spot size at the cathode, σ_l of 400 μm.

for the case of a very short laser pulse illuminating the cathode. This is due to the fact that the rf focusing effect is much smaller for a very short beam and also that a pancake-shaped beam has a larger amplitude longitudinal space charge field. In order to take advantage of rf velocity bunching in the gun, the laser pulse should be stretched to a few ps to sample a few degrees of the rf wave. In the case studied here, the self-fields of the bunch dominate the longitudinal expansion and the rf wave only makes a small contribution to the final beam phase space distribution. The energy distribution chirp does not vary significantly in the relatively large interval of phases under study.

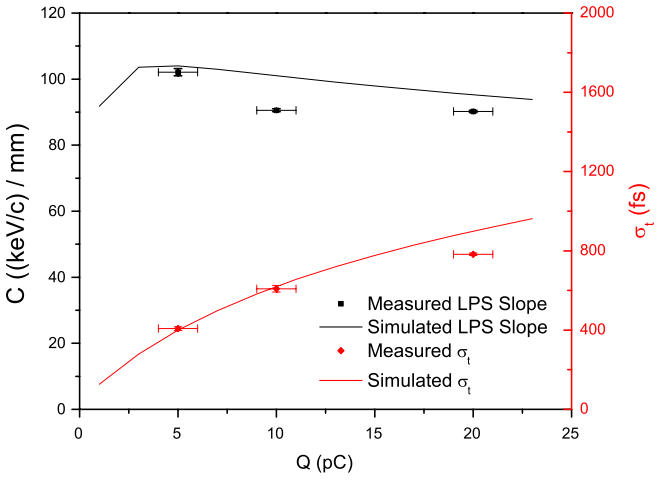

FIG. 6. (Color) A scan of the chirp (C) (left axis, black) and σ_t (right axis, red) versus beam charge. The measured values (points) are compared to simulations performed with general particle tracer (lines). The scan was performed with $\phi_0 = 22$ degrees and an initial spot size at the cathode, $\sigma_l = 500$ μm.

Even more interesting is the behavior when we vary the input charge (see Fig. 6). We observe, as expected, a significant variation in the rms bunch length and energy spread. For these measurements the initial laser spot size at the cathode was $\sigma_l = 500$ μm which explains the slightly shorter bunch lengths.

What may be less expected is the weak dependence of the chirp slope (C) on the beam charge. As the rms beam parameters increase by a factor of 2, the time-energy correlation remains quasiconstant. For a typical beam in the blow-out regime of photoinjector operation, we observe that in the one-dimensional approximation of the longitudinal expansion, the resulting analytical estimate for C [Eq. (6)] does not depend on the surface charge density at the cathode. This effect was discussed in the nonrelativistic case in [35] and it is true in the long time limit or at large enough distance from the cathode where these measurements have been performed, since it is based on the fact that the space charge expansion is nearly complete.

This ceases to be true when the approximation of space charge driven expansion of an initial pancake beam is violated. For example, at the lowest charge point, the bunch lengthening due to the space charge is minimal and other dynamical factors, for example the rf field curvature and transverse dependence, influence the beam evolution.

Finally, we have studied the LPS as a function of the laser spot size at the cathode while keeping the charge constant. Since surface charge density determines the longitudinal expansion, reducing the beam dimensions on the cathode will have a large effect on the expansion dynamics. As the initial spot size on the cathode is decreased, the bunch length increases quickly, while the slope of the chirp decreases at first weakly then more noticeably for the

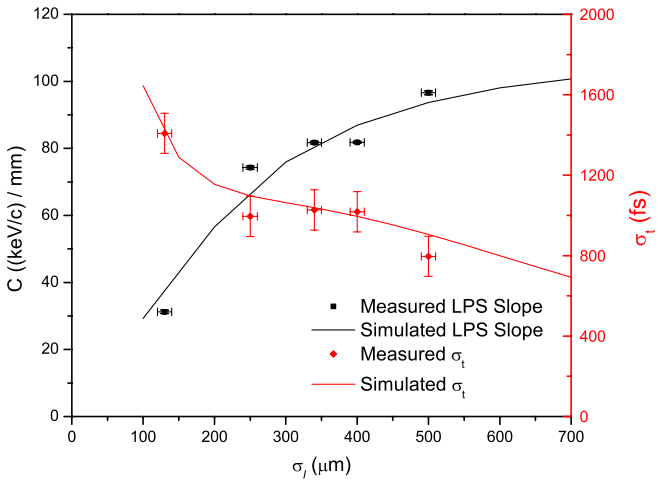

FIG. 7. (Color) A scan of the chirp (C) (left axis, black) and σ_t (right axis, red) versus σ_l. The measured values (points) are compared to GPT simulations. The scan was performed with 20 pC of charge and an rf gun phase of $\phi_0 = 22$ degrees.

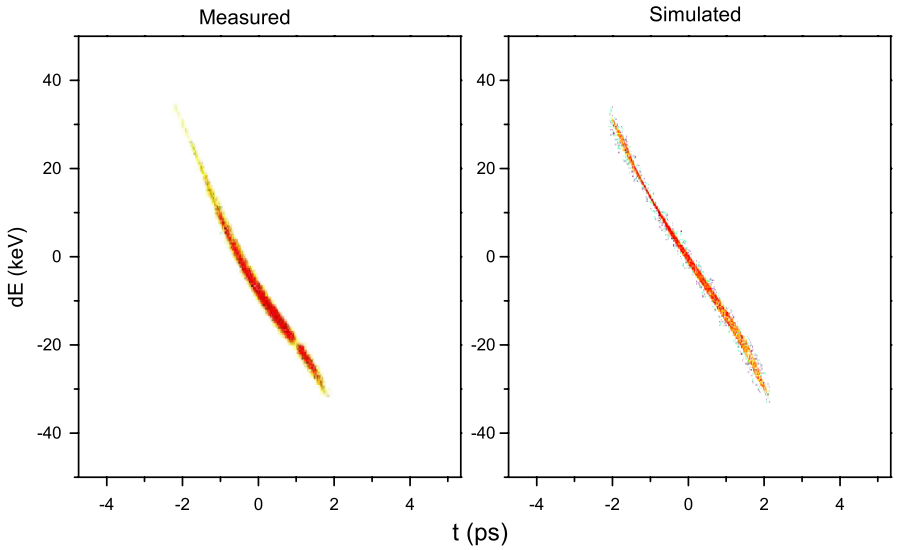

FIG. 8. (Color) An example of nonlinearity in the longitudinal phase space. The measured LPS is shown on the left while the GPT simulated LPS is shown on the right. The nonlinearity in the LPS can be attributed to asymmetry in the beam caused by image charges due to high charge density at the cathode. These shots were taken with a charge of 20 pC and an rms transverse spot size at the cathode of $\sigma_l = 130$ μm.

smaller spot sizes. This can be explained by observing that a smaller chirp is due to a relatively longer beam and smaller energy spread. The longitudinal space charge force decreases more rapidly for smaller laser spot at the cathode due to the fact that the beam (longer and transversely smaller) exits the pancake regime after a shorter propagation distance. In this situation, which by definition is not accounted for in the approximation leading to Eq. (6), the energy spread growth rate diminishes quickly, leading to a final state with a lower energy chirp.

Examining more closely at the complete LPS distribution of the smallest laser spot size data point in Fig. 7, we observe the onset of beam quality degradation due to asymmetry discussed in Ref. [10]. When the surface charge density approaches 10% of the rf accelerating field, the space charge induced expansion becomes asymmetric due to image charge effects. In Fig. 8 we show the measured and simulated LPS beam distributions. The effect is quite dramatic with the beam distribution losing its nearly ideal linear correlation. Projecting the beam distribution onto the time axis, one finds an asymmetric shape. Such a density profile is the self-consistent cause for the curvature in the self-field dominating the phase space distribution in Fig. 8. The distortion at the tail of the beam can be attributed to the ''retarding'' effect of the image charge that lowers the energy of the beam tail.

V. CONCLUSION

The longitudinal phase space of the beam in the blow-out regime of rf photoinjector has been studied at the UCLA Pegasus laboratory. In order to fully characterize the beam, a high resolution longitudinal phase space diagnostic based on a vertically deflecting rf cavity and a horizontally dispersing dipole has been implemented. A relative slice energy spread lower than 0.03% was found corresponding to an absolute value of 1.0 keV. This resolution was obtained by careful management of longitudinal-transverse correlations introduced by the rf deflector as described by the Panofsky-Wenzel theorem. The low $<$0.5 mm mrad longitudinal emittance measured emphasizes the nearly ideal behavior of the uniformly filled ellipsoidal beam distribution created by the space charge driven expansion of a pancake-shaped beam.

We have also analyzed the relative ineffectiveness of rf bunching when very short laser pulses hit the cathode. For larger surface charge densities, the image charge induced asymmetry of the expansion has been observed, which leads to a degradation of the LPS distribution linearity.

An experiment to compress a beam generated in the blow-out regime at this point would be an important step for accessing the applications that need a high brightness ultrashort beam.

ACKNOWLEDGMENTS

Special acknowledgements go to R. J. England for the construction of the rf deflecting cavity, Radiabeam for use of the IBIS YAG, and D. Filippetto for insightful comments. This work was supported by ONR Award No. N000140711174 and DOE Grant No. DE-FG02-92ER40693.

[1] J. Arthur *et al.*, SLAC Report No. SLAC-R-593, 2002, http://www-ssrl.slac.stanford.edu/lcls/.

[2] Desy Report No. TESLA FEL 2002-09, edited by R. Brinkmann *et al.* (2002).
[3] W. Brown *et al.*, Phys. Rev. ST Accel. Beams **7**, 060702 (2004).
[4] J. Hastings *et al.*, Appl. Phys. Lett. **89**, 184109 (2006).
[5] P. Musumeci *et al.*, Ultramicroscopy **108**, 1450 (2008).
[6] M. Ferrario *et al.*, SLAC Report No. SLAC-PUB-8400, 2000.
[7] C. Limborg-Deprey and P. R. Bolton, Nucl. Instrum. Methods Phys. Res., Sect. A **557**, 106 (2006).
[8] O. J. Luiten *et al.*, Phys. Rev. Lett. **93**, 094802 (2004).
[9] L. Serafini, in *Towards the X-Ray Free Electron Laser*, edited by R. Bonifacio and W. A. Barletta, AIP Conf. Proc. No. 413 (AIP, New York, 1997), p. 321.
[10] P. Musumeci, J. T. Moody, R. J. England, J. B. Rosenzweig, and T. Tran, Phys. Rev. Lett. **100**, 244801 (2008).
[11] I. M. Kapchinskii and V. V. Vladimirskii, in *Proceedings of the International Conference on High Energy Accelerators* (CERN, Geneva, 1959), p. 274.
[12] K. J. Kim, Nucl. Instrum. Methods Phys. Res., Sect. A **275**, 201 (1989).
[13] B. E. Carlsten, Nucl. Instrum. Methods Phys. Res., Sect. A **285**, 313 (1989).
[14] L. Serafini and J. B. Rosenzweig, Phys. Rev. E **55**, 7565 (1997).
[15] J. Ronsch *et al.*, prepared for the 7th European Workshop on Beam Diagnostics and Instrumentation for Particle Accelerators (DIPAC 2005), Lyon, France, 2005.
[16] H. Loos *et al.*, Nucl. Instrum. Methods Phys. Res., Sect. A **528**, 189 (2004).
[17] P. Emma, J. Frish, and P. Krejcik, Report No. LCLS-TN-00-12, 2000.
[18] X. J. Wang in *Proceedings of the 18th Particle Accelerator Conference, New York, 1999* (IEEE, New York, 1999).
[19] M. Roehrs, C. Gerth, M. Huning, and H. Schlarb, in *Proceedings of the 10th European Particle Accelerator Conference, Edinburgh, Scotland, 2006* (EPS-AG, Edinburgh, Scotland, 2006).
[20] R. Richter *et al.*, in *Proceedings of the 2007 Particle Accelerator Conference, Albuquerque, New Mexico, 2007* (IEEE, Albuquerque, New Mexico, 2007), p. 3967.
[21] D. Alesini, Int. J. Mod. Phys. A **22**, 3693 (2007).
[22] P. Emma, Z. Huang, K. J. Kim, and P. Piot, Phys. Rev. ST Accel. Beams **9**, 100702 (2006).
[23] R. J. England *et al.*, in *Proceedings of the 2006 Advanced Accelerator Concepts Workshop*, AIP Conf. Proc. No. 887 (AIP, New York, 2006), p. 595.
[24] P. Musumeci, J. T. Moody, M. S. Gutierrez, and C. M. Scoby, Rev. Sci. Instrum. **80**, 013302 (2009).
[25] D. Filippetto, M. Bellaveglia, P. Musumeci, and C. Ronsivalle, Nucl. Instrum. Methods Phys. Res., Sect. A **605**, 215 (2009).
[26] A. Mostacci *et al.*, Rev. Sci. Instrum. **79**, 013303 (2008).
[27] M. P. Stockli, R. F. Welton, and R. Keller, Rev. Sci. Instrum. **75**, 1646 (2004).
[28] J. B. Rosenzweig, *Fundamentals of Beam Physics* (Oxford University Press, New York, 2003), p. 100.
[29] W. K. H. Panofsky and W. A. Wenzel, Rev. Sci. Instrum. **27**, 967 (1956).
[30] S. B. van der Geer, M. J. de Loos, T. Van Oudheusden, W. P. E. M. op t Root, M. J. van der Wiel, and O. J. Luiten, Phys. Rev. ST Accel. Beams **9**, 044203 (2006).
[31] T. van Oudheusden, E. F. de Jong, S. B. van der Geer, W. P. E. M. Op 't Root, O. J. Luiten, and B. J. Siwick, J. Appl. Phys. **102**, 093501 (2007).
[32] Z. Huang *et al.*, Phys. Rev. ST Accel. Beams **7**, 074401 (2004).
[33] Z. Huang, D. Dowell, P. Emma, C. Limborg-Deprey, G. Stupakov, and J. Wu, in *Proceedings of the 21st Particle Accelerator Conference, Knoxville, 2005* (IEEE, Piscataway, NJ, 2005), p. 3570.
[34] X. J. Wang, X. Qiu, and I. Ben-Zvi, Phys. Rev. E **54**, R3121 (1996).
[35] W. E. King *et al.*, J. Appl. Phys. **97**, 111101 (2005).